HAIDI Instrument Details and DOAS Spectral Analysis

The HAIDI near-limb spectrometer recorded spectra with a resolution of roughly 0.55 nm FWHM in the range 301–408 nm. Three measurement spectra were coadded to reduce noise while maintaining good temporal resolution of 3 s for each observation. For the DOAS fit, reference spectra were often selected from the highest altitude portions of flights, generally around 1 km. For the 26 flights with data from the forward spectrometer, 15 unique reference spectra were used.

5

Fit Range	331.8 - 369.6 nm
Reference Spectrum	Recorded near max flight altitude
Polynomial	3rd-order
Ring Spectra	Bussemer (1993), Quadratic Expansion
BrO	Fleischmann et al. (2004) 273K
NO_2	Bogumil et al. (2003) 243K
O_4	Thalman and Volkamer (2013) 253K
O_3	Serdyuchenko et al. (2014) 243K and 273K
OClO	Kromminga et al. (2003) 213K

Table S1. Fit parameters for the retrieval of BrO, NO_2, and O_4 dSCDs.

The fit parameters are shown in Table S1. The fit routine includes three Ring spectra, with a quadratic expansion, to account for rotational Raman scattering and its nonlinear impacts, using the methods from Bussemer (1993). The fit did not include HCHO, as it has a similar spectral structure to BrO, and fit uncertainties were reduced when it was not included. In testing, it was found not to have a large impact on the retrieved dSCDs, likely due to the remote location and clean atmosphere. Even in plumes downwind of Prudhoe Bay fossil fuel facilities, HCHO was not identified with confidence (i.e. dSCDs were below the detection limit). Further, final BrO dSCDs are lower in observations of these plumes, indicating that the omission of HCHO has little impact on BrO dSCDs, even in the few areas where we might expect HCHO.

10
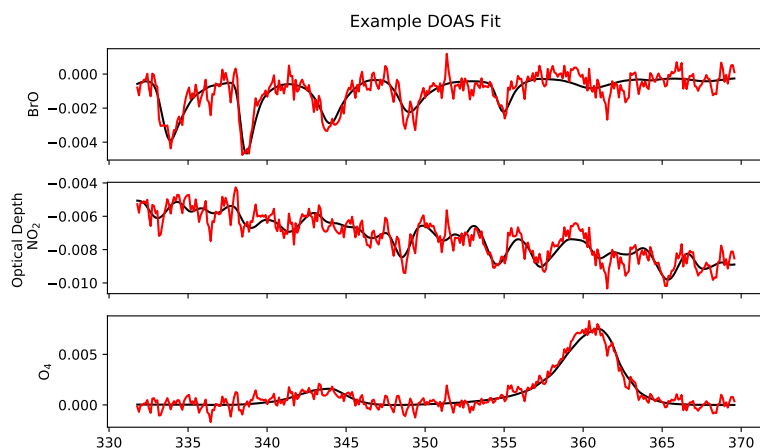
Figure S1. A typical dSCD fit result for BrO, NO_2, and O_4 with the absorption cross-section in black and the cross-section plus the fit residual in red. NO_2 and BrO fits result in negative coefficients, indicating more trace gas absorption in the measurement spectrum than the reference spectrum. Alternatively, there is less O_4 absorption in the measurement spectrum due to light cutoff by the surface, as this measurement was made at 140 m altitude and a viewing angle of $-1.85°$.

The fit routine resulted in dSCDs for BrO, NO$_2$, and O$_4$ with detection limits of roughly 3.3×10^{13} molecules/cm^2, 2.8×10^{15} molecules/cm^2, and 1.4×10^{42} molecules^2/cm^5 based on median 2σ uncertainties. A typical dSCD retrieval is shown in Fig. S1.

AMAX-DOAS Theory
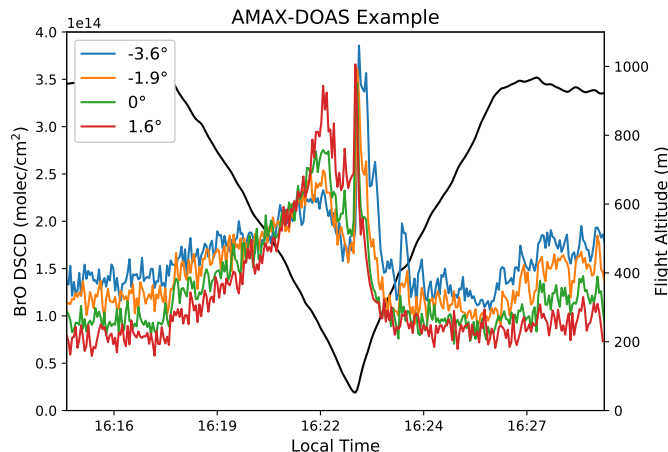
Figure S2. dSCD results from each viewing angle for an example atmospheric profile, where the listed viewing angles are relative to the aircraft. ALAR descended with a mean pitch angle of -3.8° in the left half of this figure, as seen by the altitude shown in black. During this time, the upward-most viewing angle (red) had the largest dSCD increase due to having the longest light path lengths through the lower atmosphere. Similarly, as the aircraft began to rise with a pitch angle of +4.7°, the largest dSCDs were observed in the lowest viewing angle for the same reason.

A subset of data from a single porpoise is shown in Fig. S2 to display the different sensitivity each viewing angle has, with the observations from the four different viewing angles shown in the colored lines. The relative viewing angles are listed in the legend, however as the aircraft descends and ascends, the absolute viewing angle will change with the aircraft pitch angle. As the aircraft starts its descent with a mean pitch angle of -3.8°, all four observations show increasing BrO dSCDs, peaking near the bottom of this profile in the highest viewing angle, which is near-limb due to the negative pitch angle of the aircraft. However, as the aircraft ascends with a pitch angle of +4.7°, the lowest viewing angle is the nearest-limb observation resulting in that viewing angle observing the highest dSCDs. These observations indicate higher BrO concentrations toward the surface, however this is clearly a qualitative discussion. For quantitative results, we need to couple these observations to radiative transfer modelling.

Radiative Transfer Model Initialization

Temperature and pressure were constrained with data from the aircraft for available flight altitudes for a given day. Temperatures above the maximum altitude were linearly interpolated to a 215 K tropopause located at 9 km. The temperature was then held constant up to 29 km altitude before linearly increasing with altitude to 245 K at 48 km. The hypsometric approximation was used to calculate pressures above the maximum flight altitude.

A standard profile for ozone and NO$_2$ was scaled for each flight day based on the Ozone Monitoring Instrument total ozone column and tropospheric/total NO$_2$ column observations (Veefkind, 2012; Krotkov et al., 2019). The stratospheric BrO profile was determined from the Theys et al. (2009) climatology, based on the mean flight solar zenith angles, total ozone column, and

stratospheric NO_2 column. Tropospheric BrO was set to 0.5 pmol mol^{-1} through the free troposphere, 1 pmol mol^{-1} between
500 and 700 m, 2.5 pmol mol^{-1} between 300 and 500 m, and 10 pmol mol^{-1} below 300 m. No diurnal variation was applied
to the BrO profile, as flights were often near solar noon and lasted less than 4.5 hours. This BrO profile is also used as the
apriori BrO profile for the BrO mixing ratio optimal estimation algorithm. Apart from these three trace gases, O_4 absorption
and Rayleigh scattering are also included in VLIDORT calculations.

40   The particle loading was split into two particle types representing the upper atmosphere (above 6 km) and the lower atmosphere (below 6 km). The stratospheric particle loading was determined from the The Global Space-based Stratospheric Aerosol Climatology (Kovilakam et al., 2020) based on the measurement month and assuming a clean atmosphere. The aerosol particle extinction for the free troposphere was set to a constant 0.015 km^{-1}.

    The particle extinction profile for the lower atmosphere was determined by first calculating a number density concentration from the Grimm particle counter (model 1.109) on ALAR (briefly described in Peterson et al. 2017) for each observation. This
45 number density was then used to determine a mean particle profile shape from throughout each flight. The profile shape was then scaled to the total AOD from nearby Aeronet observations (Holben et al., 2001). This apriori particle extinction profile was then used as the input for the O_4 particle inversion to determine the final particle extinction profile of each flight. The Grimm only measures the particle size distribution (PSD) down to 0.25 µm. As the most optically relevant particles for UV-Vis remote sensing are smaller than 0.25 µm, we chose to use the number density as opposed to the surface area as the latter parameter
50 would skew toward larger particles with less optical relevance to UV-Vis DOAS observations.

    The optical properties for these two particle types were determined with a bulk Mie code, specifically designed for use with VLIDORT. The PSD for upper atmosphere particles was taken from Nyaku et al. (2020) based on their unimodal lognormal distribution fits and averaged over all altitude ranges. The refractive indices cited in Kovilakam and Deshler (2015) were also used here, with a wavelength-independent imaginary refractive index of 5×10^{-3}. Both the PSD and refractive indices of lower
55 atmosphere particles were taken from Aeronet Version 3.0, Level 1.5 preliminary data (Sinyuk et al., 2020). Any missing data was set as the mean for the observation period. Considering that all particles considered were highly scattering and that the particle extinction inversion algorithm ensures the model matches observations, this preliminary data is likely not a significant source of uncertainty. The refractive indices and PSDs were then input to a bulk Mie code to produce aerosol scattering and extinction coefficients and moments. These results are used by VLIDORT to determine the angular scattering distribution as
60 well as convert particle extinction between different wavelengths. Again, Grimm data was not used for the PSD input, as the instrument misses particles smaller than 0.25 µm.

    VLIDORT operated at a wavelength of 350 nm for BrO and NO_2 observations (361 nm for O_4) and assumed a constant surface albedo of 0.825. This assumption could be incorrect for observations near sea ice leads. However, HAIDI forward-viewing observations show little impact on the intensity in the near-limb spectrometer when darker surfaces are underneath the
65 aircraft. Although, this assumed albedo would need to be updated for nadir modelling. To save computational time, VLIDORT only simulated observations during the aircraft profiling of the atmosphere (Fig. 1), as well as several hand-selected areas of interest, resulting in roughly 60% of the observed spectra being modelled. For each simulation, a box air mass factor (BAMF) is calculated for each of the forward viewing angles, based on the aircraft pitch angle, aircraft altitude, and solar geometry.

    Formally, the BAMF is defined as the partial derivative of the SCD with respect to the partial trace gas vertical column:

70
$$BAMF_i = \frac{\partial SCD}{\partial N_i} \tag{1}$$

where N is the partial vertical column density of the ith layer. The SCD can therefore by approximated by:

$$SCD = \sum_{i=1}^{n} BAMF_i \cdot C_i \cdot \Delta h_i \tag{2}$$

where Δh is the height of the ith grid cell and C is the trace gas concentration in that cell.

O_4 Inversion and Particle Extinction Profile Retrieval

75 Numerous techniques for solving the inverse problem to determine atmospheric parameters based on remote sensing observations are detailed in Rodgers (2000), and the specific method used here is based on the work of Baidar et al. (2013). The

inversion technique relies on a forward model Jacobian matrix, such that

$$\boldsymbol{y} = \mathbf{K}\boldsymbol{x} + \varepsilon \tag{3}$$

where $\boldsymbol{y}$ is the measurement vector, $\boldsymbol{x}$ is the state vector we wish to retrieve, and ε is the combination of modelled and measured
error. The forward model ($\mathbf{K}$) describes the sensitivity of the measurement vector to the state parameter, and takes the form:

$$\mathbf{K} = \frac{\partial \boldsymbol{y}}{\partial \boldsymbol{x}}. \tag{4}$$

However, there is a nonlinear relationship between the particle extinction profile and the observed O_4 SCD, thus necessitating
an iterative approach.

O$_4$ DOAS observations can be used to inverse model particle extinction profiles, where the Jacobian matrix takes the form:

$$\mathbf{K} = \frac{\partial \boldsymbol{SCD_{O_4}}}{\partial \varepsilon_i}. \tag{5}$$

We can rearrange the Lambert-Beer law to define the SCD as:

$$SCD = \frac{1}{\sigma} \ln \frac{I_0}{I} \tag{6}$$

where I_0 is the intensity of light without the given absorber and σ is the absorption cross-section of the trace gas. By using this
definition, we can calculate the Jacobian matrix as:

$$\mathbf{K} = \frac{1}{\sigma}\left(\frac{1}{I_0}\frac{\partial I_0}{\partial \varepsilon_i} - \frac{1}{I}\frac{\partial I}{\partial \varepsilon_i}\right) \tag{7}$$

where I_0 refers to a modelled radiance without O_4 absorption. The parameter $\frac{\partial I}{\partial \varepsilon_i}$ is the particle extinction Jacobian calculated
by VLIDORT for a model run at 361 nm, which is in the middle of an O_4 absorption peak, with the model initialized as
described in the previous section. This Jacobian describes how the particle extinction at each altitude impacts the modelled
radiance at the observer both with (I) and without (I_0) O_4 absorption. As HAIDI retrieves dSCDs for each observation,
we calculate the residual slant column density of the reference spectrum by running VLIDORT for the reference spectrum
solar/measurement geometry to convert each observation to an SCD to use as the measurement vector ($\boldsymbol{y}$).

For the O_4 inversion, we utilized the Levenberg-Marquardt method (Levenberg, 1944; Marquardt, 1963), which is an iterative
damped least-squares optimization where:

$$\boldsymbol{x_{i+1}} = \boldsymbol{x_i} + [(1+\gamma)\mathbf{S_a}^{-1} + \mathbf{K_i^T}\mathbf{S_\epsilon}^{-1}\mathbf{K_i}]^{-1}[\mathbf{K_i^T}\mathbf{S_\epsilon}^{-1}(\boldsymbol{y} - \hat{y}) - \mathbf{S_a}^{-1}(\boldsymbol{x_i} - \boldsymbol{x_a})]. \tag{8}$$

This numeric solution is a function of the apriori particle extinction profile ($\boldsymbol{x_a}$), apriori error matrix ($\mathbf{S_a}$), the observations ($\boldsymbol{y}$),
measurement error matrix ($\mathbf{S_\epsilon}$), and the modelled SCD ($\hat{y}$) and Jacobian matrix ($\mathbf{K_i}$) calculated with the previous extinction
profile (x_i). The apriori extinction profile is described above, and the uncertainty is set at 50% below 2 km and 2.5% above 2
km. This uncertainty profile ensures that the inversion will have a larger impact on the altitudes in which the observations are
most sensitive. The diagonals of $\mathbf{S_a}$ are the squares of this uncertainty. The off-diagonal values are set at:

$$\mathbf{S}_{a_{ij}} = \sqrt{\mathbf{S}_{a_{ii}} \cdot \mathbf{S}_{a_{jj}}} exp\left(-\ln(2) \cdot \left(\frac{Z_i - Z_j}{\delta}\right)^2\right) \tag{9}$$

where Z is the altitude grid and δ is a correlation length used to link nearby altitudes and smooth the resulting profile (described
in Hendrick et al. 2004). In the O_4 inversion, a value of $\delta = 50$ m is used.

The tuning parameter (γ) is used to increase the step size when the cost function is large and decrease the change in the
retrieved profile as a minimum cost function is approached. We start with a γ of 0.01 and decrease by a factor of two if the cost
function decreases and increase by a factor of 5 if the cost function increases. The cost function is defined as:

$$\chi^2 = (y - \hat{y})^T \mathbf{S}_{\delta\hat{\mathbf{y}}}^{-1}(y - \hat{y}) \tag{10}$$

where

$$\mathbf{S}_{\delta\hat{\mathbf{y}}} = \mathbf{S}_\epsilon(\hat{\mathbf{K}}\mathbf{S_a}\hat{\mathbf{K}}^{\mathbf{T}} + \mathbf{S}_\epsilon)^{-1}\mathbf{S}_\epsilon. \tag{11}$$

The algorithm is run at most eight times, though no run hit this threshold, until the cost function falls below $2\text{x}10^{90}$, a number determined by trial and error. The cost function is so large because O_4 SCDs are typically on the order of 10^{43} molec^2/cm^5. More commonly, the algorithm stopped as the particle extinction profile no longer significantly changed between iterations, which occurred if the mean relative difference below 1 km altitude between the current and prior extinction profiles was less than 10%.

BrO inversion

The combination of all BrO dSCD observations from each porpoise flight profile, down and up, were used for individual inversions to calculate BrO profiles (i.e. one BrO profile for each porpoise), which is solved via:

$$x = [\mathbf{K^T}\mathbf{S}_\epsilon^{-1}\mathbf{K} + \mathbf{S_a}^{-1}]^{-1}[\mathbf{K^T}\mathbf{S}_\epsilon^{-1}\boldsymbol{y} + \mathbf{S_a}^{-1}\boldsymbol{x_a}] \tag{12}$$

where $\mathbf{K}$ now has the form:

$$\mathbf{K} = \frac{\partial SCD_{BrO}}{\partial N_{BrOi}} = \mathbf{BAMF}_i \tag{13}$$

to retrieve the vertical profile of column BrO. The resulting profile is then simply divided by the height of each grid cell to obtain a concentration profile. Again, we chose to use the SCD as the measurement vector by adding a modelled SCD_0, determined by running VLIDORT for the reference spectrum solar/measurement geometry, to the observed dSCDs.

The apriori error matrix is often used as a tuning parameter, and we vary the value based on measurement sensitivity to ensure that the inversion has the greatest impact on relevant altitudes. For altitudes in the range flown by the aircraft during a profile, the apriori uncertainty is 7.5 pmol mol^{-1}. For altitudes below this flight range that still show good measurement sensitivity (modelled BAMFs > 15), the uncertainty is set to 7.5 pmol mol^{-1}. If the modelled sensitivity is low, 2.5 pmol mol^{-1} is used. For altitudes above the flight range with good measurement sensitivity, the apriori uncertainty is 1 pmol mol^{-1}. For all other altitudes below 3 km, the uncertainty is also set to 0.25 pmol mol^{-1} and set to 0.05 pmol mol^{-1} above 3 km. This uncertainty profile ensures that the inversion has a larger impact on the altitudes with higher measurement sensitivity. Again, the off-diagonal values of this matrix are set as before, in this case with a correlation length of δ = 25 m.

Cluster Information

The choice of four BrO mixing ratio clusters was determined via the silhouette score (Fig. S3), which quantifies how much better a profile's cluster explains its shape compared to the next closest cluster. A higher silhouette score means that a certain number of clusters explains the shape of the profiles better than another number of clusters. In this case, two clusters had the highest silhouette score. However, this provided us little additional information, as the profiles were grouped into a high and low BrO mixing ratio cluster. By using the number of clusters with the second highest silhouette score (4), we learned more information about common BrO profile shapes that still accounted for the total variability of the profiles well.

The total distribution of the four mixing ratio clusters may be of use to study the distribution of the different clusters and if there was any temporal trend. The total number of each clustered profile for each flight day is shown in Fig. S4 and Table S2. Low and high surface BrO clusters were seen throughout the campaign period, indicating that there was little temporal influence on the BrO profiles.

March 19, 2022 Lofted BrO Profiles

The majority (11 of 15) of the lofted BrO profiles were retrieved on a single day, March 19, 2022. This day was noted as being more hazy than other flight days. This can be seen in Fig. S5, which shows webcam images from HAIDI for two flight days.
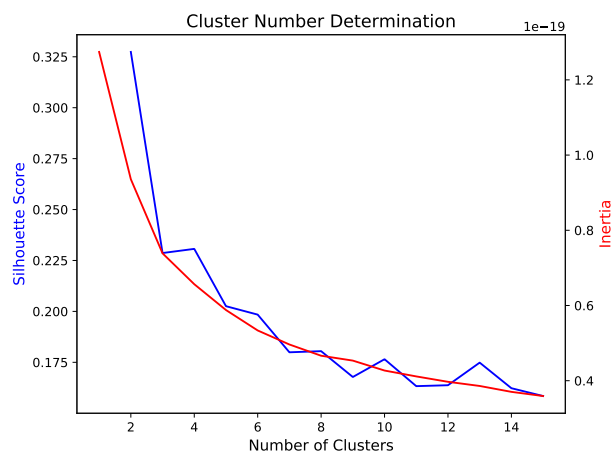
Figure S3. Results of the silhouette score test (blue) used to determine the number of clusters for the K-means analysis. We chose the second highest score of 4 clusters to get more detail about common profile shapes. The inertia (red) is also shown, although was not used to determine the number of clusters to include.
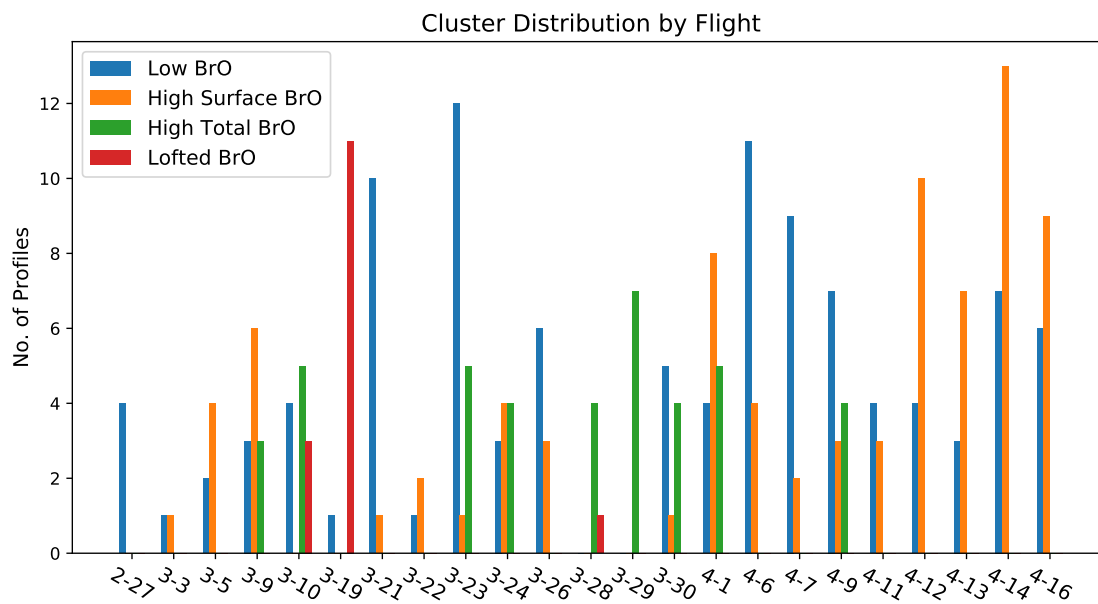
Figure S4. The distribution of each cluster as a function of flight. We saw no clear trend in the time of year that certain clusters were observed.

150   On the left is an image from March 19, 2022 where the haze is evident based on the lack of detail in the snow surface and the difficulty identifying the horizon. On the right side is a webcam image from a similar location and time of day on March 21, 2022. The visibility on this day was much better, as seen by the detail on the snow surface.

| Date	Low BrO #	High Surface BrO #	High Total BrO #	Lofted BrO #
2-27	4 (100%)	0 (0%)	0 (0%)	0 (0%)
3-3	1 (50%)	1 (50%)	0 (0%)	0 (0%)
3-5	2 (33%)	4 (67%)	0 (0%)	0 (0%)
3-9	3 (25%)	6 (50%)	3 (25%)	0 (0%)
3-10	4 (33%)	0 (0%)	5 (42%)	3 (25%)
3-19	1 (8%)	0 (0%)	0 (0%)	11 (92%)
3-21	10 (91%)	1 (9%)	0 (0%)	0 (0%)
3-22	1 (33%)	2 (67%)	0 (0%)	0 (0%)
3-23	13 (72%)	0 (0%)	5 (28%)	0 (0%)
3-24	3 (27%)	4 (36%)	4 (36%)	0 (0%)
3-26	6 (67%)	3 (33%)	0 (0%)	0 (0%)
3-28	0 (0%)	0 (0%)	4 (80%)	1 (20%)
3-29	0 (0%)	0 (0%)	7 (100%)	0 (0%)
3-30	5 (50%)	1 (10%)	4 (40%)	0 (0%)
4-1	4 (24%)	8 (47%)	5 (29%)	0 (0%)
4-6	12 (80%)	3 (20%)	0 (0%)	0 (0%)
4-7	9 (82%)	2 (18%)	0 (0%)	0 (0%)
4-9	8 (57%)	2 (14%)	4 (29%)	0 (0%)
4-11	4 (57%)	3 (43%)	0 (0%)	0 (0%)
4-12	4 (29%)	10 (71%)	0 (0%)	0 (0%)
4-13	3 (30%)	7 (70%)	0 (0%)	0 (0%)
4-14	7 (35%)	13 (65%)	0 (0%)	0 (0%)
4-16	6 (40%)	9 (60%)	0 (0%)	0 (0%)

Table S2. The total number of each BrO cluster retrieved is shown for each flight day. The percentage of each profile is listed for each day in parentheses.


Figure S5. Images from the forward viewing webcam on ALAR showing an example of the haze observed on March 19 (left) compared to a clear day (March 21, right). Both images were recorded in a similar location at a similar time of day.

ALAR Average Parameters

For clarity, the data shown in Figs. 10 and 11 did not display the variability of the averaged parameters. These parameters
155 are shown in this section (Figs. S6-S9) with their variability shown as error bars. The first parameter shown (Fig. S6) is the

7
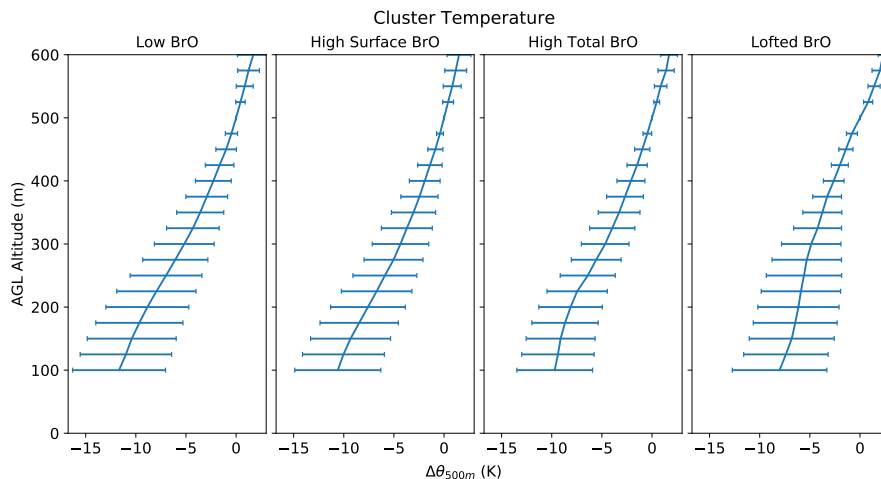
Figure S6. The standard deviation of the offset potential temperature shown in Fig. 10. The temperature at different levels is often not significantly different. However, we are more concerned with the shape of the different profiles, as this indicates the stability of the lower atmosphere.
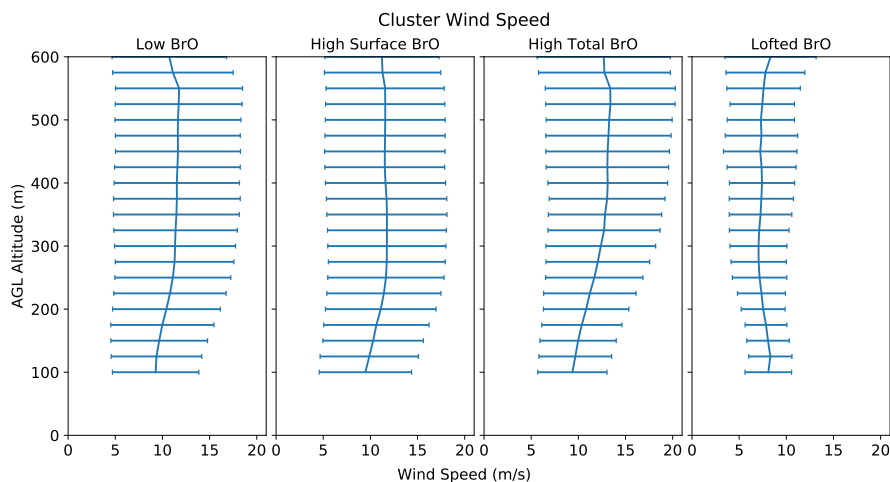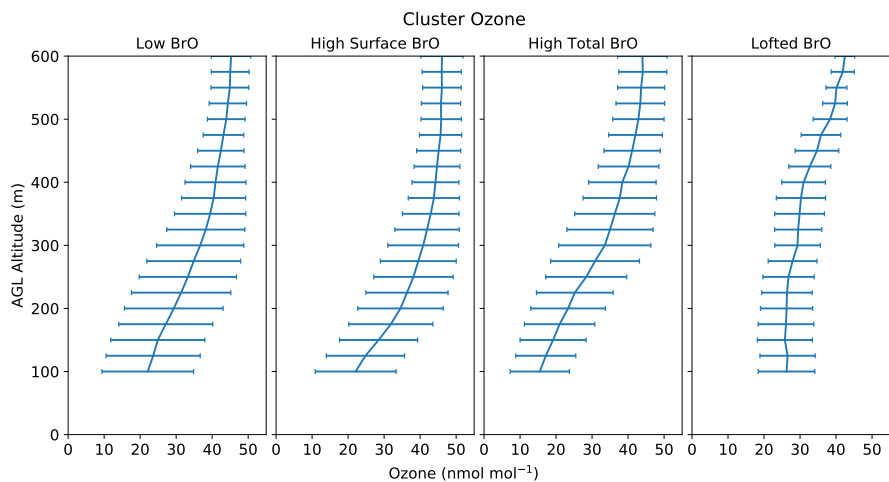

Figure S7. The standard deviation of the average cluster wind speed shown in Fig. 10.

normalized potential temperature, which is the average potential temperature offset by the potential temperature at 500 m, hence why the variability at 500 m is zero. This variability shows that the four temperature profiles do not have significantly different temperatures at most altitudes. However, this parameter was used to discuss atmospheric thermodynamic stability, so we are much more interested in the lapse rate of the lower atmosphere than the total variability of these profiles.

160   Figure S9 shows the variability of the extinction profile for each cluster. As can be seen, the extinction profiles for the low BrO and high total BrO cases has significant variability at the surface. This large variability is due to the fact that the low BrO and high total BrO clusters were observed on March 23, 2022 where a particle extinction of 2.1 km^{-1} was retrieved at the surface. This was much higher than any other day (next highest was 0.65 km^{-1}).

8

Figure S8. The standard deviation of the average ozone mixing ratio shown in Fig. 11.
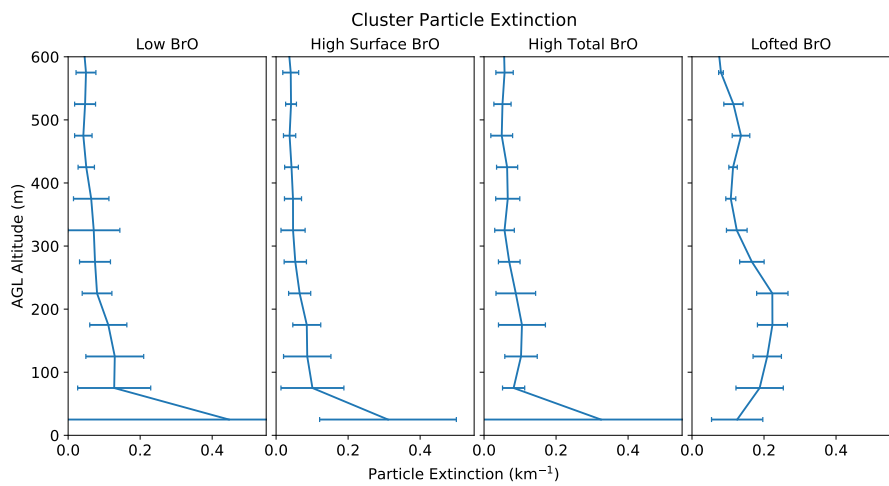
Figure S9. The standard deviation of the particle extinction profiles shown in Fig. 11. The variability at the surface for the low BrO and high total BrO cases is due to one day (March 23) with a much higher surface extinction than any other day (2 km^{-1} compared to 0.2 km^{-1} on average for all other days).

References

165   Baidar, S., Oetjen, H., Coburn, S., Dix, B., Ortega, I., Sinreich, R., and Volkamer, R.: The CU Airborne MAX-DOAS instrument: vertical profiling of aerosol extinction and trace gases, Atmos. Meas. Tech., 6, 719–739, https://doi.org/10.5194/amt-6-719-2013, 2013.

Bogumil, K., Orphal, J., Homann, T., Voigt, S., Spietz, P., Fleischmann, O. C., Vogel, A., Hartmann, M., Kromminga, H., Bovensmann, H., Frerick, J., and Burrows, J. P.: Measurements of molecular absorption spectra with the SCIAMACHY pre-flight model: Instrument characterization and reference data for atmospheric remote-sensing in the 230-2380 nm region, J. Photochem. Photobio. A, 157, 167–184,
170   https://doi.org/10.1016/S1010-6030(03)00062-5, 2003.

Bussemer, M.: Der Ring-effekt: Ursachen und einfluß auf die spektroskopische messung stratosphärischer spurenstoffe, Diplomathesis, University of Heidelberg, 1993.

Fleischmann, O. C., Hartmann, M., Burrows, J. P., and Orphal, J.: New ultraviolet absorption cross-sections of BrO at atmospheric temperatures measured by time-windowing Fourier transform spectroscopy, J. Photochem. Photobio. A, 168, 117–132,
175   https://doi.org/10.1016/j.jphotochem.2004.03.026, 2004.

Hendrick, F., Barret, B., Van Roozendael, M., Boesch, H., Butz, A., De Mazière, M., Goutail, F., Hermans, C., Lambert, J.-C., Pfeilsticker, K., and Pommereau, J.-P.: Retrieval of nitrogen dioxide stratospheric profiles from ground-based zenith-sky UV-visible observations: validation of the technique through correlative comparisons, Atmos. Chem. Phys., 4, 2091–2106, https://doi.org/10.5194/acp-4-2091-2004, 2004.

180   Holben, B. N., Tanré, D., Smirnov, A., Eck, T. F., Slutsker, I., Abuhassan, N., Newcomb, W. W., Schafer, J. S., Chatenet, B., Lavenu, F., Kaufman, Y. J., Castle, J. V., Setzer, A., Markham, B., Clark, D., Frouin, R., Halthore, R., Karneli, A., O'Neill, N. T., Pietras, C., Pinker, R. T., Voss, K., and Zibordi, G.: An emerging ground-based aerosol climatology: Aerosol optical depth from AERONET, J. Geophys. Res. Atmos., 106, 12 067–12 097, https://doi.org/https://doi.org/10.1029/2001JD900014, 2001.

Kovilakam, M. and Deshler, T.: On the accuracy of stratospheric aerosol extinction derived from in situ size distribution measurements and
185   surface area density derived from remote SAGE II and HALOE extinction measurements, J. Geophys. Res. Atmos., 120, 8426–8447, https://doi.org/https://doi.org/10.1002/2015JD023303, 2015.

Kovilakam, M., Thomason, L. W., Ernest, N., Rieger, L., Bourassa, A., and Millán, L.: The Global Space-based Stratospheric Aerosol Climatology (version 2.0): 1979–2018, Earth Syst. Sci. Data, 12, 2607–2634, https://doi.org/10.5194/essd-12-2607-2020, 2020.

Kromminga, H., Orphal, J., Spietz, P., Voigt, S., and Burrows, J.: New measurements of OClO absorption cross-sections in the
190   325–435 nm region and their temperature dependence between 213 and 293 K, J. Photochem. Photobio. A, 157, 149–160, https://doi.org/https://doi.org/10.1016/S1010-6030(03)00071-6, 2003.

Krotkov, N. A., Lamsal, L. N., Marchenko, S. V., Celarier, E. A., J.Bucsela, E., Swartz, W. H., Joiner, J., and the OMI core team: OMI/Aura NO2 Total and Tropospheric Column Daily L2 Global Gridded 0.25 degree x 0.25 degree V3, https://doi.org/10.5067/Aura/OMI/DATA2018, 2019.

195   Levenberg, K.: A method for the solution of certain non-linear problems in least squares, Q. Appl. Math., 2, https://doi.org/10.1090/qam/10666, 1944.

Marquardt, D. W.: An Algorithm for Least-Squares Estimation of Nonlinear Parameters, J. Soc. Ind. Appl. Math., 11, https://doi.org/10.1137/0111030, 1963.

Nyaku, E., Loughman, R., Bhartia, P. K., Deshler, T., Chen, Z., and Colarco, P. R.: A comparison of lognormal and gamma size distributions
200   for characterizing the stratospheric aerosol phase function from optical particle counter measurements, Atmos. Meas. Tech., 13, 1071–1087, https://doi.org/10.5194/amt-13-1071-2020, 2020.

Peterson, P. K., Pöhler, D., Sihler, H., Zielcke, J., General, S., Frieß, U., Platt, U., Simpson, W. R., Nghiem, S. V., Shepson, P. B., Stirm, B. H., Dhaniyala, S., Wagner, T., Caulton, D. R., Fuentes, J. D., and Pratt, K. A.: Observations of bromine monoxide transport in the Arctic sustained on aerosol particles, Atmos. Chem. Phys., 17, 7567–7579, https://doi.org/10.5194/acp-17-7567-2017, 2017.

205   Rodgers, C. D.: Inverse methods for atmospheric sounding: Theory and Practice, Series on Atmospheric, Oceanic and Planetary Physics–Vol. 2,, vol. 2, World Scientific Publishing, Singapore, 2000.

Serdyuchenko, A., Gorshelev, V., Weber, M., Chehade, W., and Burrows, J. P.: High spectral resolution ozone absorption cross-sections – Part 2: Temperature dependence, Atmos. Meas. Tech., 7, 625–636, https://doi.org/10.5194/amt-7-625-2014, 2014.

Sinyuk, A., Holben, B. N., Eck, T. F., Giles, D. M., Slutsker, I., Korkin, S., Schafer, J. S., Smirnov, A., Sorokin, M., and Lyapustin, A.:
210   The AERONET Version 3 aerosol retrieval algorithm, associated uncertainties and comparisons to Version 2, Atmos. Meas. Tech., 13, 3375–3411, https://doi.org/10.5194/amt-13-3375-2020, 2020.

Thalman, R. and Volkamer, R.: Temperature dependent absorption cross-sections of O2-O2 collision pairs between 340 and 630 nm and at atmospherically relevant pressure., Phys. Chem. Chem. Phys., 15, 15 371–81, https://doi.org/10.1039/c3cp50968k, 2013.

Theys, N., Roozendael, M. V., Errera, Q., Hendrick, F., Daerden, F., Chabrillat, S., Dorf, M., Pfeilsticker, K., Rozanov, A., Lotz, W., Burrows, J. P., Lambert, J.-C., Goutail, F., Roscoe, H. K., and Mazière, M. D.: A global stratospheric bromine monoxide climatology based on the BASCOE chemical transport model, Atmos. Chem. Phys., 9, 831–848, https://doi.org/10.5194/acp-9-831-2009, 2009.

Veefkind, P.: OMI/Aura Ozone (O3) DOAS Total Column L3 1 day 0.25 degree x 0.25 degree V3, https://doi.org/10.5067/Aura/OMI/DATA3005, 2012.

215